Nitrogen-doped graphenic foam synthesized by solvothermal-based process: Effect of pyrolysis temperature on the material properties

Lilian Moumaneix, Sébastien Fontana, M. Dossot, François Lapicque, Claire Hérold

Nitrogen-doped graphenic foam synthesized by solvothermal-based process: Effect of pyrolysis temperature on the material properties

Lilian Moumaneix[1], Sébastien Fontana[1], Manuel Dossot[2], François Lapicque[3], Claire Hérold[1*]

[1] Institut Jean Lamour, CNRS –Université de Lorraine, 2 allée André Guinier, 54011 Nancy, France

[2] Laboratoire de Chimie Physique et microbiologie pour les Matériaux et l'Environnement, CNRS – Université de Lorraine, 405 rue de Vandoeuvre, 54600 Villers les Nancy, France

[3] Laboratoire Réactions et Génie des procédés, CNRS – Université de Lorraine, ENSIC, 54000 Nancy, France

Abstract:

Extraordinary properties of graphenic materials no longer need to be demonstrated. Nitrogen doping has been known to broaden the graphene application fields, especially for catalysis purposes. The present work reports a solvothermal-based process for the synthesis of a nitrogen-doped graphenic foam with up to 2.6 at.% nitrogen, exhibiting the inherent properties of graphenic materials with high textural properties and surface areas as high as 2243 $m^2.g^{-1}$. This study aims to give a better understanding of the influence of the pyrolysis treatment on the properties of the produced material for optimization of the synthesis in view to fuel cell applications. Several cross-linked techniques such as transmission electron microscopy, thermogravimetric analysis, Raman spectroscopy, nitrogen physisorption at 77 K and X-ray photoelectron spectroscopy have been employed to give a complete, precise characterization of the elaborated N-doped graphenic foams, leading to optimized conditions for the pyrolysis step. Pyrolysis at 850 °C has been found to allow the best compromise in terms of purity, homogeneity and crystallinity, with high fractions of pyrrolic, pyridinic and graphitic N-substitution that are known to greatly enhance the material catalytic properties. An oxidative degradation process was also evidenced for temperatures above 875 °C, leading to far lower graphene amounts.

Keywords: graphene foam; solvothermal-based process; nitrogen doping; synthetic microporous material; surface characterization

***Corresponding author:** Dr. Claire Herold claire.herold@univ-lorraine.fr +33372742537

1. Introduction

Since its validation in 2004 by Geim and Novoselov [1,2], graphene has stimulated wide interest due to its outstanding properties including perfect sp^2 carbon structure, large conjugated system, charge carrier mobility higher than 200,000 $cm^2.V^{-1}.s^{-1}$ [3,4], thermal conductivity reaching 5300 $W.m^{-1}.K^{-1}$ [5], high theoretical specific surface area of 2630 $m^2.g^{-1}$ [6], Young's modulus of 1 TPa [7] associated with flexibility [8], high transparency, extreme thinness, impermeability to liquids and gases [9] and potentially low production cost. Mostly known for its applications in nanodevices such as field effect transistors [10], transparent electrodes [11], ultracapacitors [12] or photoelectric [13], extensive studies have also shown great promise for applications in flexible energy storage devices [14], drug carrier [15] or wearable functional devices [16,17].

Graphene is a two-dimensional basic building block which forms many carbon materials such as (0D) fullerenes through wrapping, (1D) carbon nanotubes (CNT) via rolling, (3D) graphite by stacking, as well as carbon nanoribbons, quantum dots, etc. Graphene can easily be tailored in many ways to form graphene-based materials with specific morphology and chemical functionalization, adapted to specific applications. Studies have shown that it was possible to use graphene-based materials to progress in many different fields of science e.g. energy storage [18], sensors [19], bio-applications [19], oxygen reduction reactions in fuel cells [20], batteries (including metal-air batteries and Li-ion batteries) [21] or nanodevices.

Graphene has the specificity to be a zero-bandgap material, its conduction and valence bands meet at the Dirac points, on the edge of the Brillouin zone. Semiconducting properties are highly searched to improve some applications such as high on/off ratio field effect transistors [22] or increase the conductivity of transparent electrodes. Doping is a common strategy for carbon materials, it notably permitted to widely expand the applications of CNT. Among numerous doping atoms (e.g. boron, sulfur, oxygen, phosphorous), nitrogen is a very promising candidate as its integration into the graphene network involves partial redistribution of the electric charge of the atoms, due to the difference of electronegativity between nitrogen atoms and carbon atoms, respectively 3.04 and 2.55 on Pauling scale [23]. Moreover, doping with nitrogen atoms transforms graphene into p- or n-type semiconductor, in related to the opening of the bandgap [24]. N-doped graphene alone exhibits activity toward oxygen reduction reactions in both acidic and alkaline media and thus has been studied as a cathode catalyst in low temperature fuel cells [25, 26]. As a support of metal particles, N-doped carbon provides nucleation sites for metal nanoparticles on N-neighboring carbon atoms and it improves the dispersion and surface area of the metal nanoparticles resulting in good performances in

catalysis e.g. for hydrogenation, coupling reactions, oxygen reduction, alcohol oxidation and in photocatalysis [27].

From a structural point of view, the integration of nitrogen atoms inside the graphene network is facilitated thanks to the low difference of atomic radius between nitrogen atoms (70 pm) and carbon atoms (77 pm). Moreover, nitrogen atoms have five valence electrons that can be used to form strong covalent bonds with carbon atoms in doped graphene layers. They can be classified into five main species: pyrrolic, pyridinic, graphitic (or quaternary), aminic and nitrogen oxides, as shown in Figure 1.

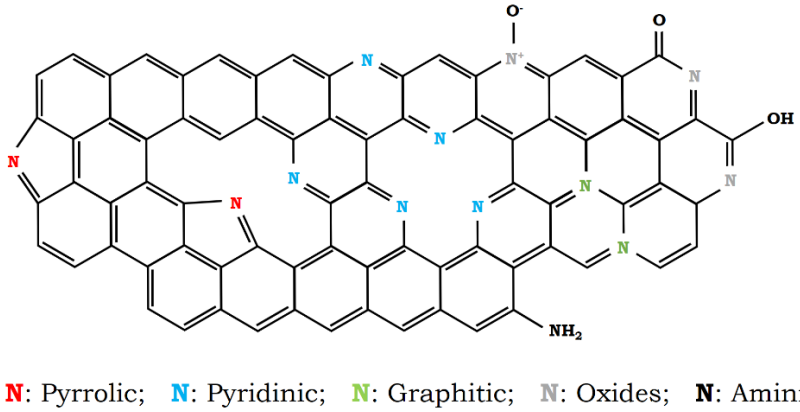

Figure 1: Schematic representation of different nitrogen functions

Pyrrolic-N (sp^3 hybridized) and pyridinic-N (sp^2 hybridized) are bonded with two carbon atoms as members of pentagon and hexagon respectively, both occurring at the edge of the layer or at the inside of the layer if coupled with vacancies. Pyrrolic-N donates two p electrons to the π system, while pyridinic-N donates one p electron. Graphitic-N substitutes one C atom and is therefore part of hexagon inside the graphenic network. Theoretically, two configurations should be considered, near the edge of the layer and within the bulk of the layer, named "valley" and "center" respectively, although no quantitative assessment has been yet reported. Aminic-N and nitrogen oxides can be found mostly at the edges of the layer [28].

Two synthesis ways leading to N-doped carbon materials are usually categorized as direct synthesis on one hand and post treatment on the other hand. Direct synthesis involves the introduction of nitrogen atoms source at the same time as carbon atoms source. This category regroups together methods such as arc-discharge-based synthesis [29], chemical vapor deposition (CVD) [30] or solvothermal-based synthesis [31]. As for post treatment, the integration of nitrogen atoms takes place after the synthesis of carbon material. Among others,

thermal treatment [32], plasma treatment [33] or the hydrazine hydrate method [34] can be listed. Each of these methods possesses intrinsic advantages and drawbacks, different scalabilities and lead to different kinds of N-doped carbons.

Solvothermal-based processes take advantage of the high flexibility of the technology, allowing large ranges of temperature and pressure as well as many possible solvents. Depending on the desiring objective, the solvent can be used as a mediator to perform a specific reaction, e.g. exfoliation of graphite, intercalation into graphite, reduction of graphene oxide [35], or can be part of the reagents and participate in the reaction. Here, a solvothermal-based process has been developed for the preparation of N-functionalized graphene that could exhibit enough catalytic properties in view to further fuel cell applications. In the literature, solvothermal reactions for N-doped graphenic materials are often based on the use of tetrachloromethane (CCl_4) in a mixture with lithium nitride (Li_3N) [36], Li_3N and cyanuric chloride $(NCCl)_3$ [37] or with pyrrole (C_4H_5N) and metallic potassium [25]. The formation of undesirable chlorine-based gases along with unavoidable nitrogen-based gases could nonetheless be bypassed by slight modifications in the used reagents and the reaction conditions. In this work, a formerly developed solvothermal route relying upon the action of reductive Na on ethanol [38-40], has been modified: here sodium is put in contact with a mixture of cyclohexanol and ethanolamine to produce a crystalline nitrogen-doped graphenic foam. Still poorly represented in publications, solvothermal-based processes have been shown to allow the synthesis of outstanding carbon materials with specific surface areas greater than 2000 $m^2.g^{-1}$, close to the theoretical value attributed to graphene monolayer. To our knowledge, no crystalline N-doped graphenic material exhibiting such a high surface area has been yet reported in literature, usual surface areas for comparable N-doped graphenic materials being below 1000 $m^2.g^{-1}$ or slightly above, e.g. 170 $m^2.g^{-1}$ [41], 413.6 $m^2.g^{-1}$ [25], 585 $m^2.g^{-1}$ [42], 719 $m^2.g^{-1}$ [43], 1209 $m^2.g^{-1}$ [31]. It is hoped that the association of inherent graphene properties with good textural properties can genuinely be an asset for fuel cell catalysts applications. This paper focus on the better understanding of the pyrolysis treatment in order to optimize the synthesis of N-doped graphenic foam for the targeted application. For this purpose, numerous cross-linked techniques have been used for accurate characterization of the prepared materials, in terms of structural, microstructural, textural and chemical properties.

2. Materials and methods

2.1.Synthesis

2.1.1 Solvothermal reaction

A mixture of 0.1 mol of cyclohexanol (Sigma Aldrich, 99%), 0.1 mol of ethanolamine (Aldrich chemistry, >99.5%) was put in contact with 0.26 mol of metallic sodium (Merck Millipore) under inert atmosphere (nitrogen Air Liquide, alphagaz 2) in a 0.5 L Parr autoclave. Cyclohexanol and ethanolamine were used as received. Sodium rods were washed in petroleum ether to remove the paraffin oil then cut in small pieces and stored under nitrogen atmosphere. Sodium pieces were scraped before being used to remove the passivation layer that is formed even under protective atmosphere. The autoclave is sealed and nitrogen (Air Liquide, alphagaz 2) was introduced so that the pressure attained 70 bar. The reactor was then heated up to 350 °C at 8 °C.min^{-1}, the internal pressure reached 200 bar, and the mixture was let to react for 72 h. Afterwards, the reaction was allowed to cool down naturally to room temperature, and the solvothermal product was collected under nitrogen atmosphere.

2.1.2 Pyrolysis

About 5 g of solvothermal product was placed in an Inconel® 600 crucible and then introduced in a vertical tubular oven. Depending on the planned conditions, the oven was heated at a heating rate of 20 °C.min^{-1} up to the reaction temperature in the range 750 °C - 900 °C for 4 h, then cooled down to room temperature naturally. The crucible was permanently kept under a nitrogen flow (Air Liquide, alphagaz 1) to avoid combustion of the carbonaceous phase and to eliminate pyrolysis gases. The pyrolysis product consisted of a greyish black powder, with in some cases sodium carbonate and sodium hydroxide white crystals.

2.1.3 Washing

The pyrolysis product was crushed then sonicated 10 min in 200 mL of distilled water. The powder was washed alternatively with 1 L 6 mol.L^{-1} hydrochloric acid (Sigma Aldrich, ≥37%) and 1 L distilled water. The initially grey powder turned to black due to the removal of sodium carbonate and sodium hydroxide formed during the pyrolysis. The washed sample was finally dried at 100 °C for 24 h, weighed and stored under air before their accurate characterization.

2.2.Characterization

Transmission electron microscopy (TEM) investigations were performed with a Jeol CM 200 microscope running at 200 kV. Samples were previously dispersed in absolute ethanol and deposited on a copper grid with a holey carbon film.

Thermogravimetric analysis (TGA) were carried out under dry air in a Setsys Evolution Setaram thermobalance. Samples were heated at 1000 C° in a platinum crucible with a heating rate of 3 C°.min^{-1} then cooled down to room temperature at 20 °C.min^{-1}. Accuracy in the masses is close to 0.1%.

Raman spectroscopy investigations were conducted with a Renishaw inVia Quontor equipped with a 532 nm laser operating in the spectral range 100-3600 cm^{-1} in synchroscan mode. Samples were first dispersed in absolute ethanol then deposited on a glass slide.

X-ray photoelectron spectroscopy (XPS) analysis were achieved with a Kratos Axis Ultra DLD, using an Al Kα1 X-ray source (1486.6 eV). C-C and C-H bounds were taken as C 1s signal references at 284.6 eV. Analyzed surface is of 700x300 µm^2 for 5-10 nm deep.

Physisorption of nitrogen at 77 K was performed with a Micromeritics ASAP2020 adsorption apparatus. The samples were outgassed during 12 h at 300 °C before analysis. Specific surface areas were calculated using the BET (completed with the Rouquerol correction) and 2D-NLDFT models, micropore volumes and pore size distributions are obtained using 2D-NLDFT model: this model can actually avoid overestimation of the specific surface area by the BET model for microporous solids. 2D-NLDFT calculations were carried out using SAIEUS software, with a corrugation parameter λ=4.25 and an integration range from 0.4 nm to 29.3 nm.

Techniques for electrical and electrochemical characterizations are presented in the Supplementary Information.

3. Results and discussion

3.1.Solvothermal reaction

Employed for the first time by Choucair *et al.* in 2009 [44], the solvothermal based process for the synthesis of graphenic foam has been used in numerous works since then. Initially, a 1:1 molar ratio of sodium and ethanol was heated in a sealed reactor vessel at 220 °C for 72 h.

Temperature was chosen to be close to the critical temperature of ethanol (240.85 °C) and the auto-generated pressure exceeded the critical pressure of ethanol (61.4 bar) during the synthesis.

In this work, as different reagents have been used, different parameters had to be chosen. If the critical point of cyclohexanol is well-known i.e. 351.85 °C, 37.5 bar, the one for ethanolamine has been estimated around 360 °C ± 40 °C and 66 bar ± 2 bar from former experimental works and calculations [45-48]. Here, the solvothermal reaction temperature was chosen slightly under the critical temperatures at 350 °C. Knowing that reducing metals react with alcohols to give the corresponding metal alkoxide, a ratio of one sodium atom for one alcohol function was first expected to be sufficient to assure a proper achievement of the reaction. However, the synthesis conducted with these parameters led to oily solvothermal products. Further experiments showed that an excess of sodium leads to homogeneous solid products and a ratio of 1.3 sodium atom per alcohol function has been chosen as a standard. Similarly, experiments carried out at 100 bar led to oily solvothermal products, which is why the pressure of 200 bar has been conserved for all synthesis.

3.2. Influence of the pyrolysis temperature

3.2.1. Pyrolysis yields

The pyrolysis temperature has been varied in the range of 750 °C - 900 °C, leading to preparations of samples N-Gr/750 to N-Gr/900. From previous studies [49], it is expected that lower temperature would lead to the formation of a material containing a significant amount of amorphous carbon. As shown by Figure 2, the yield of pyrolysis, defined as the ratio of the mass submitted to pyrolysis and the mass recovered after the washing step, was in all cases lower than 6.5 wt.%. Temperatures above 900 °C were not investigated because of the fast decrease in reaction yield with increasing temperature. This yield was found to be below 1 wt.% after pyrolysis carried out at 900 °C.

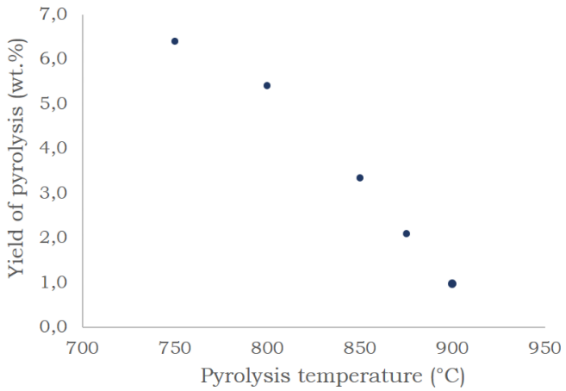

Figure 2: Evolution of pyrolysis yield with pyrolysis temperature

3.2.2. Electronic microscopy investigations

Figure 3 shows transmission electronic microscopy pictures for samples pyrolyzed at 750 °C, 800 °C, 850 °C, 875 °C and 900 °C. Particles of samples N-Gr/750 and N-Gr/800 shown in Figure 3 (a) and (b) respectively, exhibit a very smooth surface but the electron diffraction diagrams do not exhibit the characteristic patterns of crystalline carbon. Moreover, numerous thick amorphous particles can be observed for both temperatures (not shown in the pictures). This observation is in accordance with former comments, low pyrolysis temperatures lead to low crystallinity materials. It is also to notice that the 3-dimensional shape is not well developed, these samples being formed of particles with a large aspect ratio. SEM observations (Figure SI-1) reveal 3D macroscopic and highly porous structures for every graphenic foams, though no quantitative information can be drawn out from the micrographs.

Figure 3 (c) shows a view of the sample N-Gr/850. At this median temperature, 3-dimensional rounded-shaped particles consisting of multiple thin and crumpled layers could be observed, as seen in the bottom right insert. The electron diffraction pattern shows the features of polycrystalline carbon materials, corresponding to the stacking of disoriented graphene layers. A few amorphous particles (not shown on Figure 3 (c)) could also be observed, evidencing incomplete crystallization at this temperature level.

Micrographs of samples N-Gr/875 and N-Gr/900 are given in Figure 3 (d) and (e) respectively. A crumpled structure like the one observed for N-Gr/850 is present in both samples but fragments of amorphous carbon are also visible over the surface. Diffraction patterns exhibit sharp circles expressing high crystallinity of the material. At these elevated temperatures, carbon atoms receive more energy from thermal agitation than at lower temperatures which leads to higher crystallinity. In the meanwhile, a larger amount of C-material is likely to be

decomposed by the occurrence of oxidation reactions with the oxygen atoms contained in the solvothermal product submitted to pyrolysis, causing low pyrolysis yields.

TEM observations suggest that a compromise must be found between crystallinity and oxidative decomposition, leading to lower yields. Operating at 850 °C seems to allow such compromise, the material produced exhibiting good structural and micro-structural properties, with a satisfactory yield near 3.5%. However, because TEM observations provide only local information, the above results must be confirmed using other characterization techniques, in view to concluding on a general trend on the influence of the pyrolysis temperature on the quality of the C-materials produced.

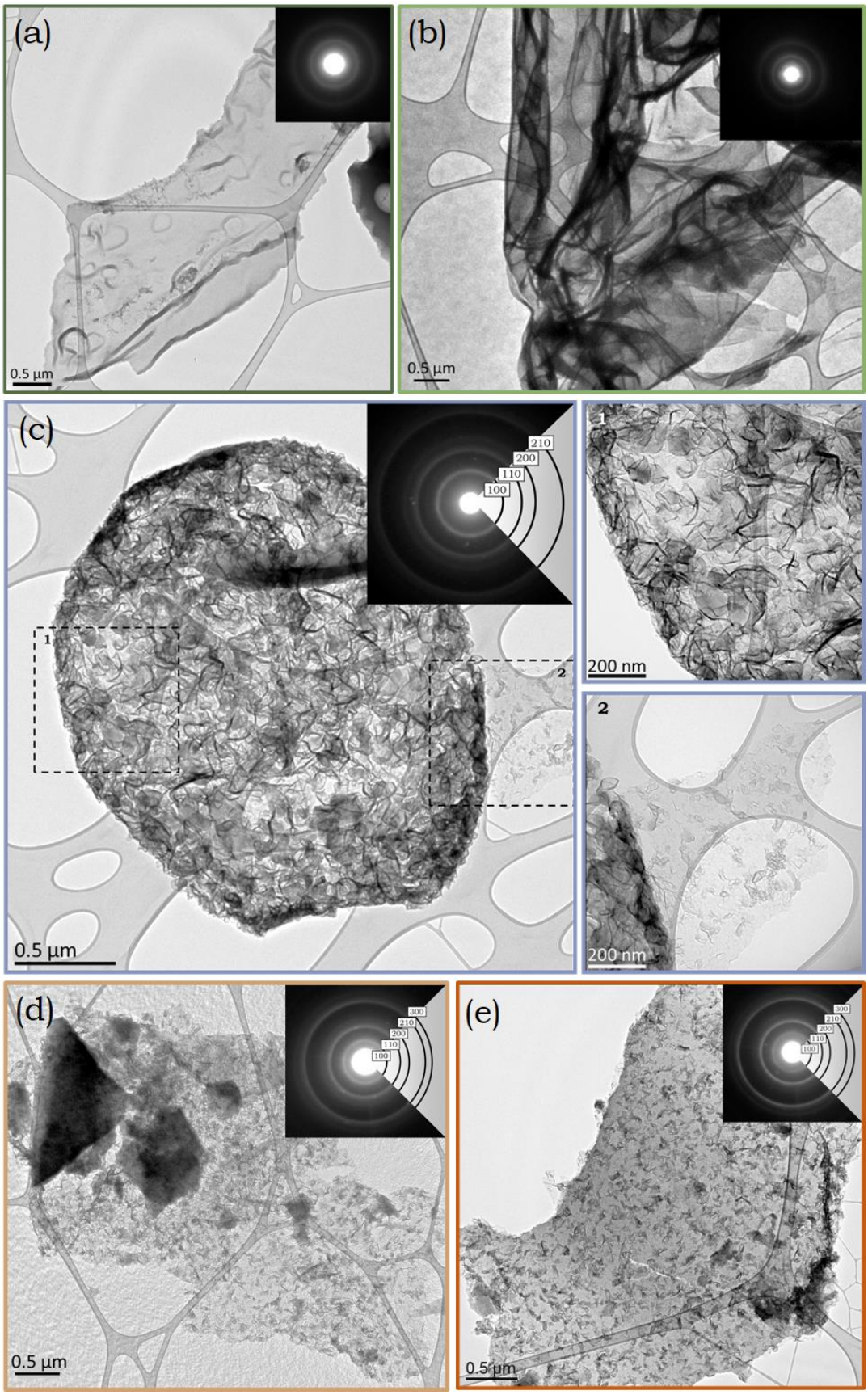

Figure 3: TEM bright-field micrographs of N-Gr/750 (a); N-Gr/800 (b;) N-Gr/850 (c); N-Gr/875 (d) and N-Gr/900 (e)

3.2.3. Thermogravimetry investigations

The five materials obtained at different pyrolysis temperatures were analyzed by thermogravimetry under dry air to estimate the homogeneity in the combustion of the carbon phase and its purity. The corresponding thermograms are given in Figure 4 in both regular (TG) and differential (dTG) mode plots.

All the thermograms present a major loss between 400 °C and 550 °C, with a single step combustion except for the highest pyrolysis temperature for which a second smaller loss is observed near 300 °C, attributed to the combustion of a low stability carbonaceous phase. Since several carbon phases have been previously evidenced by TEM observations, several losses could be expected, the amorphous phase being less stable at high temperature than the crystalline one. Thus, this single peak appearing on the differential plot combines the combustion of the different carbon phases and its full width at half maximum (FWHM) can indicate on the homogeneity of the sample, a thin peak being more likely to be related to the combustion of a single carbon phase than a wider peak. Moreover, the overall loss of matter does not reach 100% at 1000 °C as could be expected for pure carbon materials which are fully converted into carbon oxides. The final residue representing a few percent of the solid amount tested, has been identified using X-Ray Diffraction (XRD; Figure SI-2) as being mainly sodium carbonate Na_2CO_3 and a few metallic particles containing nickel or iron. Sodium carbonate progressively decomposes to sodium oxide Na_2O and carbon dioxide CO_2 above 700 °C. Figure 5 (a) shows the evolution of final weight loss (wt.%) versus the pyrolysis temperature. The less residue is obtained for N-Gr/850. At higher temperature, the quantity of sodium carbonate is higher due to the degradation of the carbon phase during the pyrolysis step while the sodium carbonate is quite stable. The higher the pyrolysis temperature, the higher the sodium carbonate over carbon material ratio. For N-Gr/900, the small peak near 720 °C in dTG curve related to the decomposition of sodium carbonate confirms the increase of this phase at high pyrolysis temperature. At pyrolysis temperatures lower than 850 °C, the poorly crystallized particles can trap sodium carbonate more easily and in larger amounts than well-crystallized particles, leading to higher residue amounts.

The temperature of combustion of the carbon phase –taken as the peak temperature shown in Figure 4b– decreases when the pyrolysis temperature increases (Figure 5 (b)). This observation is contrary to what is expected for materials with a higher crystallinity, well-crystallized particles being thermally more stable than amorphous carbon. This is directly linked to the

amount of sodium carbonate which has been shown to act as a catalyst in carbon combustion [39]. Therefore, thermogravimetric curves cannot be used for crystallinity interpretations, because of the occurrence of two unquantifiable antagonistic mechanisms.

Figure 5 (c) shows the FWHM for the DTG peaks corresponding to the major carbon loss. As mentioned above, a high FWHM value is more likely to be related with multiple carbon phases that possess close combustion temperatures, thus revealing a low homogeneity. Lowest FWHM – near 10 °C or below - are obtained for N-Gr/850 and N-Gr/875, for which the existence of a single carbon phase could be supposed. On the contrary, values of peak width over 40°C likely express the existence of several carbon phases, thus lower homogeneity of the C-materials.

Considering homogeneity and purity criteria, TGA investigations lead to an optimal pyrolysis temperature near 850 °C.

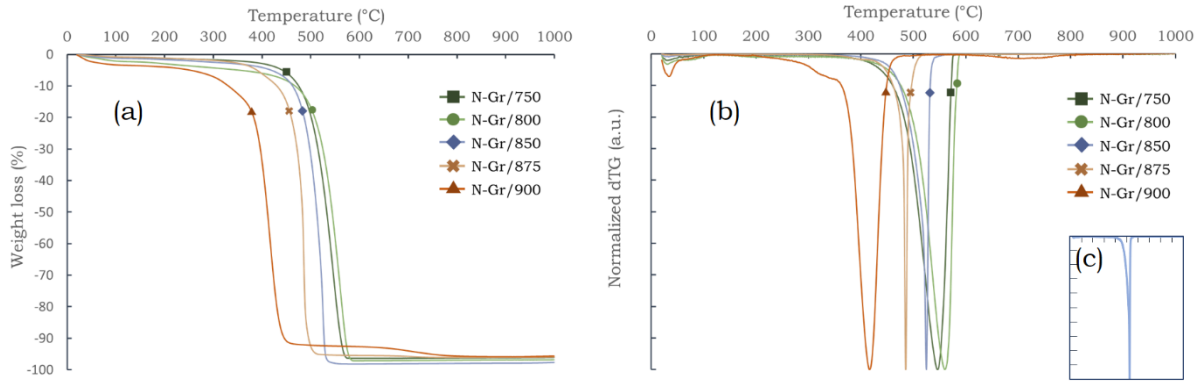

Figure 4: TG (a) and normalized dTG (b) curves (dry air, heating rate 3 °C.min^{-1}) of samples N-Gr/750 to N-Gr/900; (c) focus on dTG curve of sample N-Gr/850

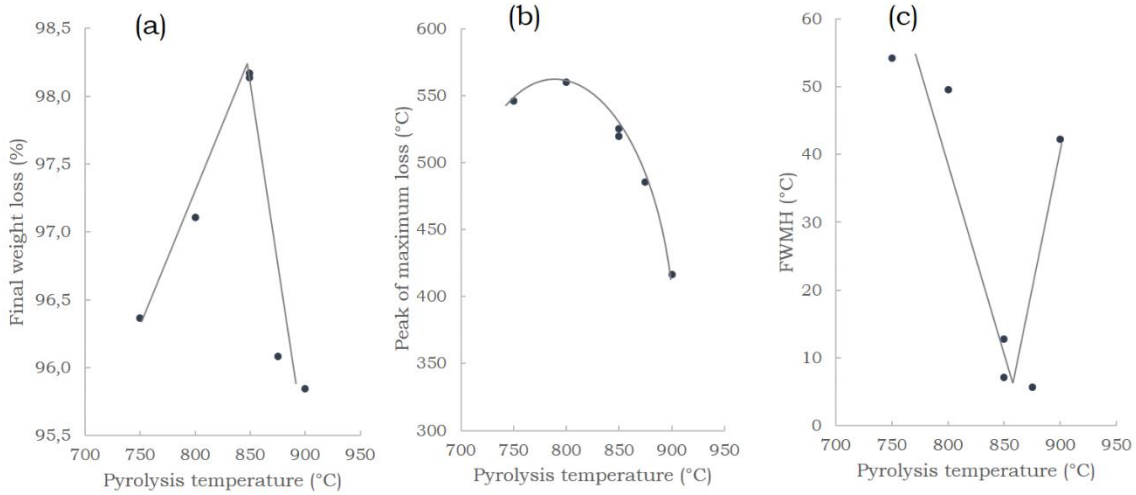

Figure 5: Evolution of final weight loss (a), peak of maximum loss (b) and FWHM (c) with pyrolysis temperature

3.2.4. Raman spectroscopy investigations

Widely used for graphenic material characterizations, Raman spectroscopy can nevertheless give rise to complex interpretations in the case of disordered materials. Raman spectra obtained for carbon materials present three major features: a D band at 1350 cm^{-1}; a G band at 1590 cm^{-1}; a G' band at 2700 cm^{-1} [50-52]. The D' band in some materials can be observed at 1620 cm^{-1} in case of disordered stacking [53]. Other contributions need to be added to achieve a proper deconvolution. Two broad bands at 1160 cm^{-1} and 1490 cm^{-1}, named bands T and F respectively [54-56], can also appear in the presence of sp^3 carbon atoms, i.e. amorphous carbon, aliphatic fraction or defects in the graphenic network. Additional overtone and combination bands were also reported at 2420 cm^{-1}, 2930 cm^{-1} and 3190 cm^{-1} [57,58]. These last bands do not give further information but can be used to confirm tendencies.

Normalized to the D band intensity Raman spectra for samples N-Gr/750 to N-Gr/900 are given by Figure 6. N-Gr/750 and N-Gr/800 present typical spectra of amorphous carbon characterized by broad D and G bands, intense defect bands, as well as a wide and low band around 2800 cm^{-1}. For N-Gr/850, N-Gr/875 and N-Gr/900, Raman spectra present some heterogeneities due to the presence of poorly to highly ordered particles. The differences in Raman spectra can be seen in Figure 7, with three different kinds of observed particles. In the following, the intermediary spectra obtained for ordered particles (cf. Figure 7 (b)) will be compared to draw general trends with the increase in pyrolysis temperature, keeping in mind that some heterogeneities can occur at these temperatures.

From a pyrolysis temperature of 850 °C and above, Raman spectra tend to present a noticeable decrease in the defect bands and a rise of both G and G' bands coupled with a narrowing of D and G bands. As pyrolysis temperature increases, these new features appear more and more clearly, possibly expressing a better crystallization at high temperature.

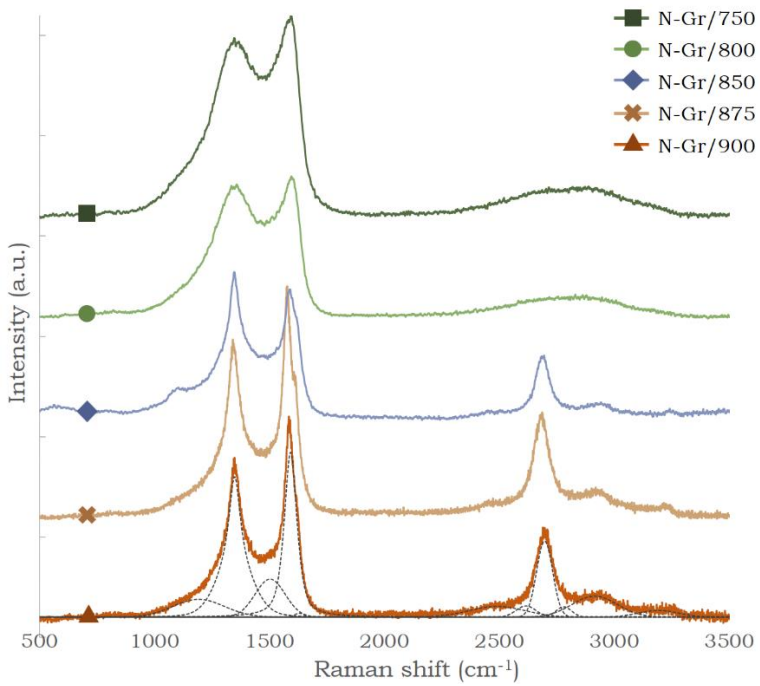

Figure 6: Normalized Raman spectra (532 nm) of samples N-Gr/750 to N-Gr/900

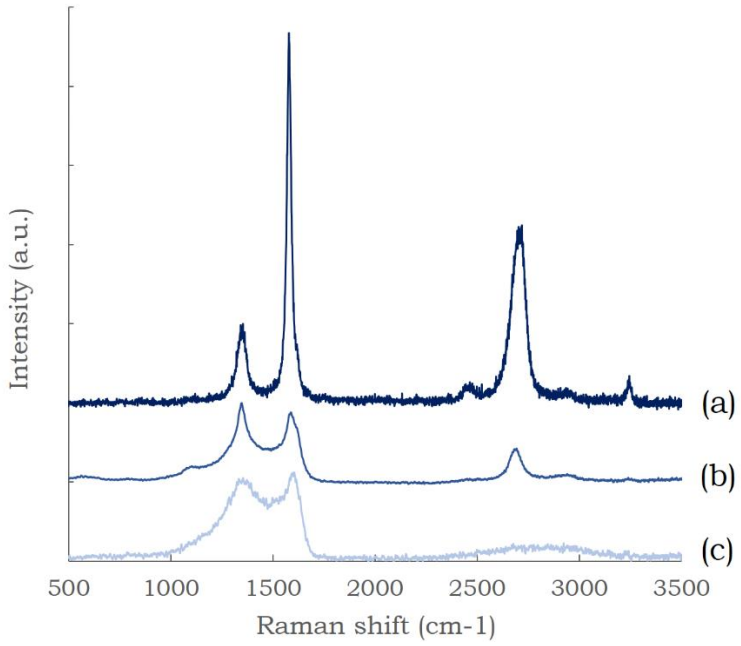

Figure 7: Normalized spectra (532 nm) of sample N-Gr/850 observed for (a) highly ordered particules; (b) ordered particules and (c) poorly ordered particules

The Raman shift of G band can be used as an indicator to follow the crystallinity of carbon materials as an increasing blue-shift is noticeable for increasing crystallinity [59]. In the same idea, the intensity ratio I_D/I_G is known to evaluate the in-plane crystallite size L_a according to the Tuinstra and Koenig (TK) equation [60]. In presence of amorphous carbon, the TK equation

is no more applicable, and the crystallinity must be studied with both I_D/I_G ratio and full width at half maximum of G band (noted FWHM(G)) [61]. Figure 8 (a) shows a constant increase in the Raman shift of G band with the increase in pyrolysis temperature which confirms that high pyrolysis temperature leads to well-crystallized materials. However, I_D/I_G ratio and FWHM(G) should have lower and lower values as crystallinity increases which is not what is observed in Figure 8 (b)(c). However, both plots follow the same tendency. As previously postulated after TEM observations, partial oxidation of carbon could explain the shape of the obtained plots. As temperature increases from 750 °C to 800 °C, I_D/I_G ratio increases due to carbon oxidation leading to higher number of defects. The sudden decrease visible at 850 °C reveals a more efficient crystallization. As temperature increases to reach 900 °C, I_D/I_G ratio rises once again due to predominance of carbon oxidation over carbon crystallization. Similar observations can be done for FWHM(G). The coexistence of crystallization and oxidation phenomena is even more likely to be confirmed by observing the evolution of defect bands with the increase in temperature. A constant diminution of defects bands is observed, especially for T and F bands, which corroborates the increase in crystallinity along with pyrolysis temperature. The optimal pyrolysis temperature appears as being around 850 °C, corresponding to the best crystallinity over oxidation compromise.

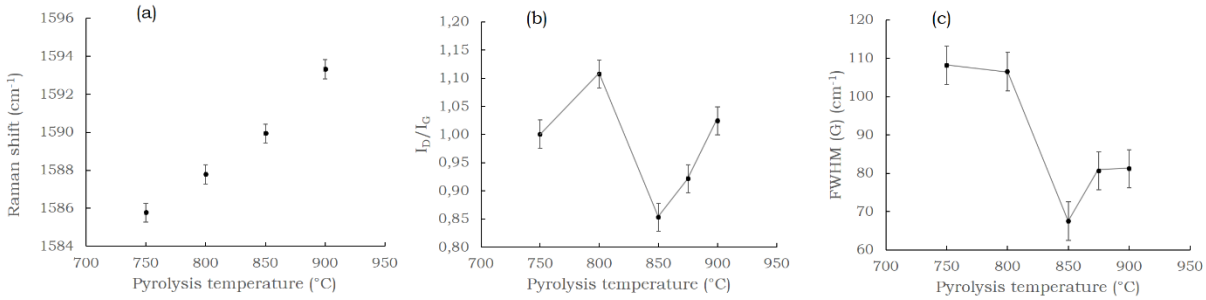

Figure 8: Evolution of G band Raman shift (a), intensity ratio I_D/I_G (b) and G band FWHM (c) with pyrolysis temperature

Speyer *et al.* [37] investigated the oxidation processes occurring during the pyrolysis of sodium alkoxide and showed that sodium interactions with carbon play a key role in the final characteristics of graphenic foam. With the increase in pyrolysis temperature, several reactions occur one after another, each one of them affecting the carbon phase structure. Under 600 °C, activation reaction (1) of carbon by sodium hydroxide promotes the expansion of microporosity and surface area due to the release of dihydrogen:

$$2\ C(s) + 6\ NaOH(l) \leftrightarrows 2\ Na(l) + 3\ H_2(g) + 2\ Na_2CO_3(s) \quad (1)$$

From 500 °C, sodium carbonate formed during reaction (1) also reacts with carbon:

$$Na_2CO_3(s) + C(s) \leftrightarrows Na_2O(s) + CO_2(g) \quad (2)$$

This reaction does not lead to additional porosity and causes partial consumption of carbon [62]. Sodium carbonate decomposition starts from 851 °C but possibly also at lower temperature in presence of carbon [63]:

$$Na_2CO_3(s) \leftrightarrows Na_2O(s) + CO_2(g) \quad (3)$$

Sodium oxides produced from reactions (2) and (3) oxidize carbon according to reaction (4):

$$Na_2O(s) + C(s) \leftrightarrows 2\ Na(g) + CO(g) \quad (4)$$

Occurring from 946 °C under Ellingham approximation, reaction (4) is likely to happen earlier due to the differences between graphite, standard reference state of carbon used for calculations, and more reactive graphenic materials. Under inert atmosphere, reaction temperature is further diminished. The increase in Na_2O concentration in the reaction medium, especially from 850°C, could explain the better elimination of disordered carbon observed in TEM, TGA and Raman analysis for samples N-Gr/850, N-Gr/875 and N-Gr/900. Furthermore, carbon degradation at pyrolysis temperature higher than 850 °C previously postulated with TEM and Raman characterizations, could be explained by the oxidation of carbon by sodium oxide at high temperature.

3.2.5. Nitrogen physisorption at 77 K investigations

Measurements of nitrogen physisorption at 77 K led to isotherms (Figure 9) with characteristic I(b), II and IV(a) isotherms as classified in the IUPAC revised recommendations [64]. The obtained profile reveals the presence of micropores with a broad distribution of size up to narrow mesopores (<2.5 nm), accompanied by intergranular mesoporosity and non-porous surfaces. The hysteresis loop reveals a capillary condensation process which generally occurs for pores wider than 4 nm [64]. The hysteresis type H4 [64] is generally observed for micro-mesoporous carbon. Micropores can be associated with an interspace between two graphenic layers, folds and tortuosity, a possible activation phenomenon due to the presence of sodium compounds or an amorphous carbon fraction.

As nitrogen is expected to be adsorbed only by the carbon atoms, specific surface areas and porous volumes have been corrected by subtracting the impurity content determined from TGA data. Specific surface areas calculated using the BET model [65, 66] as well as 2D-NLDFT

model [67] and microporous volumes obtained from the 2D-NLDFT model are presented in Table 1.

As the analyzed materials mainly have a microporous aspect, the BET model does not give accurate results for the calculation of specific surface areas. Indeed, the multilayers adsorption phenomenon assumed by this model cannot occur in too narrow pores. NLDFT model provides a better representation of adsorption as it does not rely on the multilayer adsorption assumption. Specific surface areas and microporous volumes decrease with the increase in pyrolysis temperature from 2243 m^2/g and 1.12 cm^3/g respectively to 1607 m^2/g and 0.71 cm^3/g respectively, which can be assigned to a better stacking of the graphenic layers, thus reducing the interlayer space, or to removal of amorphous carbon as previously evidenced by TGA and TEM data. Moreover, along with the increase in pyrolysis temperature, the nature of pores changes as observed by more significant nitrogen adsorption rates in middle range pressure, revealing a higher amount of non-porous areas. The study of pore size variation presented in Figure 10, shows a shift towards wider pore as well as broader pore size populations with larger pyrolysis temperatures.

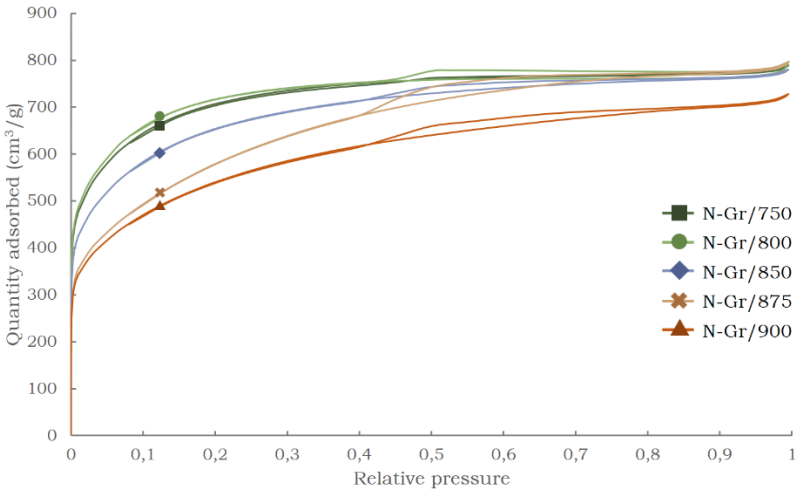

Figure 9: Adsorption isotherms (N_2, 77 K) of samples N-Gr/750 to N-Gr/900

Table 1: Specific surface area and microporous volume of samples N-Gr/750 to N-Gr/900

ID	BET surface area (m^2g^{-1})	NLDFT surface area (m^2g^{-1})	Microporous volume (cm^3g^{-1})
N-Gr750	2505	2195	1,12
N-Gr800	2555	2243	1,11
N-Gr850	2329	2006	1,13
N-Gr875	1920	1634	1,13
N-Gr900	1865	1607	1,04

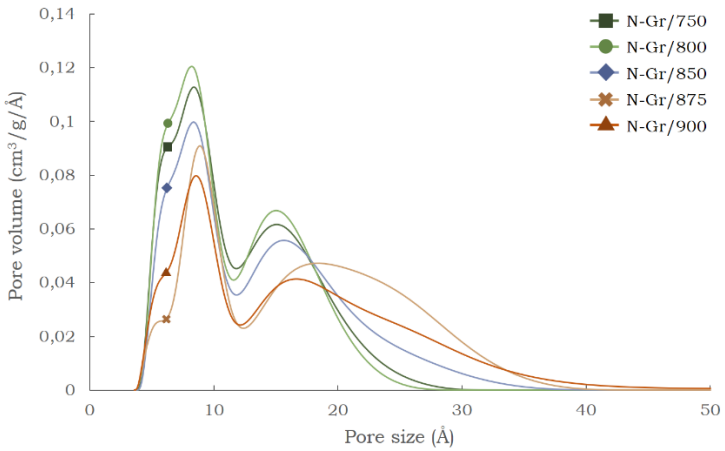

Figure 10: Evolution of pore volume with pore size for samples N-Gr/750 to N-Gr/900

3.2.6. X-Ray photoelectron spectroscopy investigations

Using X-Ray photoelectron spectroscopy (XPS), the amounts of C, N and O atoms have been determined by exploiting global spectra obtained for scanning energy ranging from 0 eV to 1100 eV. The nitrogen content was found to vary from 0.9 at.% to 2.6 at.% without a clear effect of the pyrolysis temperature. These values being close to the detection limit of the XPS analysis, the amount of nitrogen atoms was considered comparable in all samples. It has been preferred to focus on the deconvolution of XPS nitrogen core level spectrum N(1s) appearing at 400 eV, for quantitative determination of the various N species as shown in Figure 11 for N-Gr/850. The existence of five contributions has been considered, namely pyridinic-N at 398.3 eV, aminic-N at 398.9 eV, pyrrolic-N at 400.0 eV, graphitic-N at 401.4 eV and N-oxides at 402.4 eV. The possible shift around these values has been fixed at 0.3 eV to avoid artificial widening of one contribution that could overlap on another one.

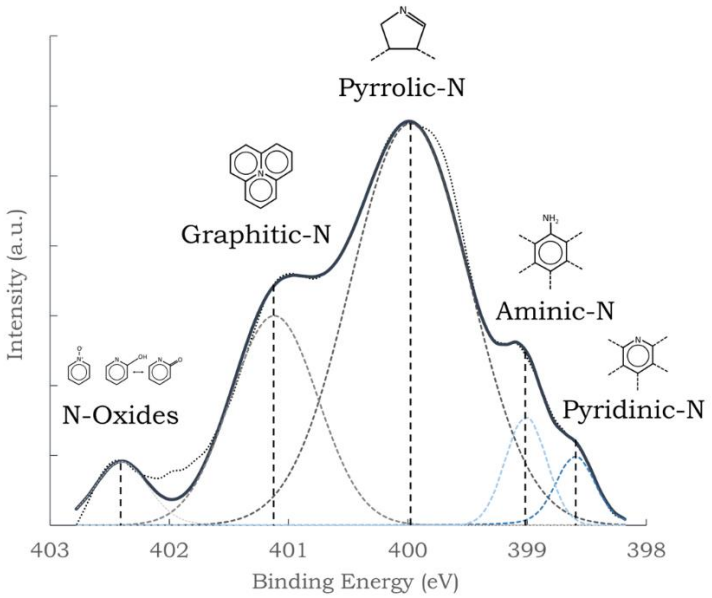

Figure 11: XPS N(1s) deconvoluted spectrum of N-Gr/850

Figure 12 makes clearly appear that pyrrolic-N functions predominate in all materials. Compared with other samples, N-Gr/750 seems to exhibit a different spectroscopic behavior than the other materials, which might be due to the lower crystallinity of the material. High quantities of pyrrolic-N are observed for higher pyrolysis temperatures, increasing from 45 at.% for N-Gr/800 to 56 at.% for N-Gr/900. Fractions of pyridinic-N functions follow comparable tendency, an increase can be observed along with higher pyrolysis temperatures, from 3 at.% for N-Gr/800 to 16 at.% for N-Gr/900. Lower fractions of graphitic-N functions were also noticed for higher pyrolysis temperature: this might result from a conversion of graphitic-N function into pyrrolic-N and pyridinic-N due to the oxidation of carbon leading to a reduction in size of carbon entities at high temperature. An important decrease in the significance of aminic-N functions is also noticed with increased pyrolysis temperature. This behavior was highly expected due to the poor thermal stability of aminic surface functions with temperature.

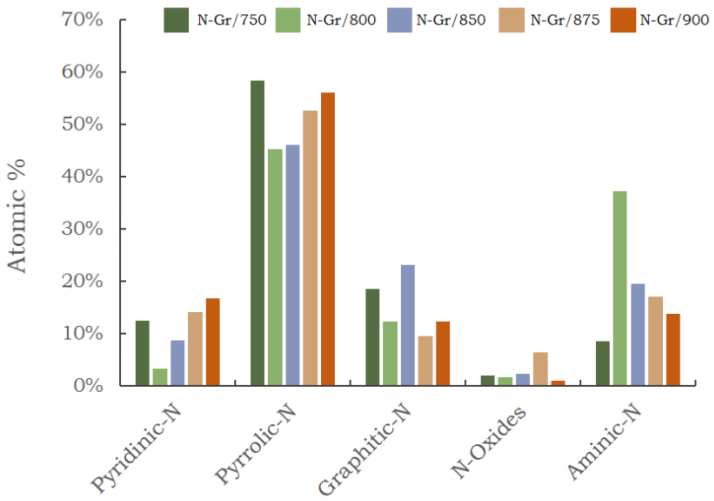

Figure 12: Evolution of nitrogen functions quantities with pyrolysis temperature

3.2.7. Electrical and electrochemical measurements

Nitrogen-doping is known to modify the electrical properties of graphenic materials [31] as it increases the number of defect sites and decreases the number of sp^2 carbon atoms. Conductivity measurements using the Van der Pauw's method (Figure SI-3) exhibit no significant differences between nitrogen-doped graphenic foam and nitrogen-free graphenic foam elaborated in a former work [49], with a conductivity of 0.40 $S.cm^{-1}$ and 0.39 $S.cm^{-1}$ respectively. This result is encouraging for future fuel cell applications.

Preliminary electrochemical measurements (Figure SI-4) show that the catalytic activity of the synthetized N-doped graphenic foams is likely to be dependent on the microstructure of the material as well as on the nitrogen doping. Very high surface area seems to provide a clear asset for ORR catalysis, as N-Gr/750 exhibit both highest power density and highest surface area, 3.2 $mW.cm^{-2}$ and 2195 $m^2.g^{-1}$ respectively. Nitrogen doping appears essential to provide a catalytic activity towards the ORR, a nitrogen-free graphenic foam showing only 0.05 $mW.cm^{-2}$ of maximum power density. Thus, coupling nitrogen-containing catalytic centers with a controlled carbon matrix microstructure seems to be the key to obtain highly performing nitrogen-doped graphenic materials for the ORR.

4. Conclusion

Nitrogen-doped graphenic foams have been successfully synthesized by a solvothermal reaction between cyclohexanol, ethanolamine and sodium followed by a pyrolysis under N_2 flow. The use of complementary techniques for the sake of thorough characterization has

permitted to achieve a better understanding of the synthesis and to determine the optimal pyrolysis temperature. XPS analysis have shown that the N-doped graphenic foams possesses 0.9 at.% to 2.6 at.% of nitrogen with up to 85% of well-inserted nitrogen functions such as pyridinic-N, pyrrolic-N and graphitic-N. The obtained NLDFT specific surface area is the highest reported to our knowledge for this kind of N-doped graphenic materials, with values as high as 2243 $m^2.g^{-1}$.

Study of the influence of pyrolysis temperature over the final product has been carried out in a range from 750 °C to 900 °C through various multi-scale characterization techniques. Pyrolysis temperature has been proved to have a critical impact on structural, microstructural and chemical properties. Increasing pyrolysis temperature tends to increase the crystallinity of the carbon phase and decrease the amount of surface N-functions but leads to higher amount of sodium carbonates that have a negative impact on the homogeneity, purity and contribute to oxidation reactions. Hence, a compromise must be found between these parameters to achieve the elaboration of an optimum material according to the most desired properties.

As reported by the present study, pyrolysis conducted at 850 °C was shown to produce the best-balanced product in terms of purity, homogeneity and ratio between crystallinity and oxidation tends to be maximum at this temperature. It has been shown that lower pyrolysis temperatures lead to poorly crystallized carbon materials with high contents of surface nitrogen functions. Above 850 °C, oxidation reactions tend to decrease the global quality of the produced material.

The comprehension of the influence of the pyrolysis step on the final product is the first step towards a more global comprehension of the whole synthesis process. Study of the solvothermal reaction step is currently in progress, since the reaction pathway remains still not well understood in the literature. Nevertheless, better understanding of both steps of the synthesis routes used, appears crucial for optimal preparation of N-doped graphenic foams, especially for electrocatalytic applications. Besides, more thorough investigations of the material performance when used as oxygen reduction catalysts in a PEM fuel cell, are presently studied: correlation between their performance in a fuel cell and their intrinsic properties will guide us for improving the design of N-doped graphenic materials.

Acknowledgments

The authors would like to thank L. Aranda from Institut Jean Lamour for his assistance in thermogravimetric analysis, and A. Renard from Laboratoire de Chimie Physique et Microbiologie pour les Matériaux et l'Environnement for his careful XPS measurements. This

work was supported partly by the french PIA project “Lorraine Université d’Excellence”, reference ANR-15-IDEX-04-LUE.

References

1. Novoselov, K. S. Electric Field Effect in Atomically Thin Carbon Films. *Science* **306**, 666–669 (2004).

2. Novoselov, K. S. *et al.* Two-dimensional gas of massless Dirac fermions in graphene. *Nature* **438**, 197–200 (2005).

3. Bolotin, K. I. *et al.* Ultrahigh electron mobility in suspended graphene. *Solid State Commun.* **146**, 351–355 (2008).

4. Morozov, S. V. *et al.* Giant Intrinsic Carrier Mobilities in Graphene and Its Bilayer. *Phys. Rev. Lett.* **100**, (2008).

5. Ghosh, S., Nika, D. L., Pokatilov, E. P. & Balandin, A. A. Heat conduction in graphene: experimental study and theoretical interpretation. *New J. Phys.* **11**, 095012 (2009).

6. Peigney, A., Laurent, Ch., Flahaut, E., Bacsa, R. R. & Rousset, A. Specific surface area of carbon nanotubes and bundles of carbon nanotubes. *Carbon* **39**, 507–514 (2001).

7. Frank, I. W., Tanenbaum, D. M., van der Zande, A. M. & McEuen, P. L. Mechanical properties of suspended graphene sheets. *J. Vac. Sci. Technol. B Microelectron. Nanometer Struct.* **25**, 2558 (2007).

8. Scarpa, F., Adhikari, S. & Srikantha Phani, A. Effective elastic mechanical properties of single layer graphene sheets. *Nanotechnology* **20**, 065709 (2009).

9. Berry, V. Impermeability of graphene and its applications. *Carbon* **62**, 1–10 (2013).

10. Vicarelli, L. *et al.* Graphene field-effect transistors as room-temperature terahertz detectors. *Nat. Mater.* **11**, 865–871 (2012).

11. Wang, X., Zhi, L. & Müllen, K. Transparent, Conductive Graphene Electrodes for Dye-Sensitized Solar Cells. *Nano Lett.* **8**, 323–327 (2008).

12. Stoller, M. D., Park, S., Zhu, Y., An, J. & Ruoff, R. S. Graphene-Based Ultracapacitors. *Nano Lett.* **8**, 3498–3502 (2008).

13. Rosli, N. N., Ibrahim, M. A., Ahmad Ludin, N., Mat Teridi, M. A. & Sopian, K. A review of graphene based transparent conducting films for use in solar photovoltaic applications. *Renew. Sustain. Energy Rev.* **99**, 83–99 (2019).

14. Gwon, H. *et al.* Flexible energy storage devices based on graphene paper. *Energy Environ. Sci.* **4**, 1277 (2011).

15. Tyagi, N., Attia, N. F. & Geckeler, K. E. Exfoliated graphene nanosheets: pH-sensitive drug carrier and anti-cancer activity. *J. Colloid Interface Sci.* **498**, 364–377 (2017).

16. Aboutalebi, S. H. *et al.* High-Performance Multifunctional Graphene Yarns: Toward Wearable All-Carbon Energy Storage Textiles. *ACS Nano* **8**, 2456–2466 (2014).

17. Wang, Y. *et al.* Wearable and Highly Sensitive Graphene Strain Sensors for Human Motion Monitoring. *Adv. Funct. Mater.* **24**, 4666–4670 (2014).

18. Pumera, M. Graphene-based nanomaterials for energy storage. *Energy Env. Sci* **4**, 668–674 (2011).

19. Shao, Y. *et al.* Graphene Based Electrochemical Sensors and Biosensors: A Review. *Electroanalysis* **22**, 1027–1036 (2010).

20. Vikkisk, M. *et al.* Electrocatalytic oxygen reduction on nitrogen-doped graphene in alkaline media. *Appl. Catal. B Environ.* **147**, 369–376 (2014).

21. Akbar, S., Rehan, M., Liu, H., Rafique, I. & Akbar, H. A brief review on graphene applications in rechargeable lithium ion battery electrode materials. *Carbon Lett.* **28**, 1–8 (2018).

22. Lu, Y. *et al.* High-On/Off-Ratio Graphene Nanoconstriction Field-Effect Transistor. *Small* **6**, 2748–2754 (2010).

23. Zhang, L. & Xia, Z. Mechanisms of Oxygen Reduction Reaction on Nitrogen-Doped Graphene for Fuel Cells. *J. Phys. Chem. C* **115**, 11170–11176 (2011).

24. Yadav, R. & Dixit, C. K. Synthesis, characterization and prospective applications of nitrogen-doped graphene: A short review. *J. Sci. Adv. Mater. Devices* **2**, 141–149 (2017).

25. Ma, R. *et al.* Novel synthesis of N-doped graphene as an efficient electrocatalyst towards oxygen reduction. *Nano Res.* **9**, 808–819 (2016).

26. Li, M., Liu, Z., Wang, F. & Xuan, J. The influence of the type of N dopping on the performance of bifunctional N-doped ordered mesoporous carbon electrocatalysts in oxygen reduction and evolution reaction. *J. Energy Chem.* **26**, 422–427 (2017).

27. Tan, H. L., Du, A., Amal, R. & Ng, Y. H. Decorating platinum on nitrogen-doped graphene sheets: Control of the platinum particle size distribution for improved photocatalytic H2 generation. *Chem. Eng. Sci.* **194**, 85–93 (2019).

28. Inagaki, M., Toyoda, M., Soneda, Y. & Morishita, T. Nitrogen-doped carbon materials. *Carbon* **132**, 104–140 (2018).

29. Panchakarla, L. S. *et al.* Synthesis, Structure, and Properties of Boron- and Nitrogen-Doped Graphene. *Adv. Mater.* NA-NA (2009). doi:10.1002/adma.200901285

30. Wang, Z. *et al.* Synthesis of nitrogen-doped graphene by chemical vapour deposition using melamine as the sole solid source of carbon and nitrogen. *J. Mater. Chem. C* **2**, 7396 (2014).

31. Choi, C. H., Park, S. H., Chung, M. W. & Woo, S. I. Easy and controlled synthesis of nitrogen-doped carbon. *Carbon* **55**, 98–107 (2013).

32. Li, D. *et al.* Facile synthesis of nitrogen-doped graphene via low-temperature pyrolysis: The effects of precursors and annealing ambience on metal-free catalytic oxidation. *Carbon* **115**, 649–658 (2017).

33. Moon, J. *et al.* One-Step Synthesis of N-doped Graphene Quantum Sheets from Monolayer Graphene by Nitrogen Plasma. *Adv. Mater.* **26**, 3501–3505 (2014).

34. Park, S. *et al.* Chemical structures of hydrazine-treated graphene oxide and generation of aromatic nitrogen doping. *Nat. Commun.* **3**, (2012).

35. Padmajan Sasikala, S., Poulin, P. & Aymonier, C. Prospects of Supercritical Fluids in Realizing Graphene-Based Functional Materials. *Adv. Mater.* **28**, 2663–2691 (2016).

36. Chen, X., Deng, D., Pan, X., Hu, Y. & Bao, X. N-doped graphene as an electron donor of iron catalysts for CO hydrogenation to light olefins. *Chemical Communications* **51**, 217–220 (2015).

37. Deng, D. *et al.* Toward N-Doped Graphene via Solvothermal Synthesis. *Chemistry of Materials* **23**, 1188–1193 (2011).

38. Speyer, L. *et al.* Multi-scale characterization of graphenic materials synthesized by a solvothermal-based process: Influence of the thermal treatment. *Solid State Sci.* **50**, 42–51 (2015).

39. Speyer, L., Fontana, S., Ploneis, S. & Hérold, C. Influence of the precursor alcohol on the adsorptive properties of graphene foams elaborated by a solvothermal-based process. *Microporous Mesoporous Mater.* **243**, 254–262 (2017).

40. Speyer, L., Fontana, S., Cahen, S. & Hérold, C. Simple production of high-quality graphene foams by pyrolysis of sodium ethoxide. *Mater. Chem. Phys.* **219**, 57–66 (2018).

41. Lyth, S. M. *et al.* Solvothermal Synthesis of Nitrogen-Containing Graphene for Electrochemical Oxygen Reduction in Acid Media. *e-Journal of Surface Science and Nanotechnology* **10**, 29–32 (2012).

42. Bayram, E., Yilmaz, G. & Mukerjee, S. A solution-based procedure for synthesis of nitrogen doped graphene as an efficient electrocatalyst for oxygen reduction reactions in acidic and alkaline electrolytes. *Applied Catalysis B: Environmental* **192**, 26–34 (2016).

43. Yang, S.-Y. *et al.* A powerful approach to fabricate nitrogen-doped graphene sheets with high specific surface area. *Electrochemistry Communications* **14**, 39–42 (2012).

44. Choucair, M., Thordarson, P. & Stride, J. A. Gram-scale production of graphene based on solvothermal synthesis and sonication. *Nat. Nanotechnol.* **4**, 30–33 (2009).

45. Li, J., Xia, L. & Xiang, S. A new method based on elements and chemical bonds for organic compounds critical properties estimation. *Fluid Phase Equilibria* **417**, 1–6 (2016).

46. Marrero, J. & Gani, R. Group-contribution based estimation o pure component properties. *Fluid Phase Equilibria* **183–184**, 183–208 (2001).

47. Scilipoti, J., Cismondi, M. & Brignole, E. A. Prediction of physical properties for molecular design of solvents. *Fluid Phase Equilibria* **362**, 74–80 (2014).

48. Tu, C.-H. Group-contribution estimation of critical temperature wih only chemical structure. *Chem. Eng. Sci.* **50**, 3515–3520 (1995).

49. Speyer, L. PhD Thesis, Université de Lorraine, Nancy (2016

50. Sasaki, K., Tokura, Y. & Sogawa, T. The Origin of Raman D Band: Bonding and Antibonding Orbitals in Graphene. *Crystals* **3**, 120–140 (2013).

51. Nemanich, R. J. & Solin, S. A. First- and second-order Raman scattering from finite-size crystals of graphite. *Phys. Rev. B* **20**, 392–401 (1979).

52. Dresselhaus, M. S., Jorio, A. & Saito, R. Characterizing Graphene, Graphite, and Carbon Nanotubes by Raman Spectroscopy. *Annu. Rev. Condens. Matter Phys.* **1**, 89–108 (2010).

53. Eckmann, A. *et al.* Probing the Nature of Defects in Graphene by Raman Spectroscopy. *Nano Lett.* **12**, 3925–3930 (2012).

54. Piscanec, S., Mauri, F., Ferrari, A. C., Lazzeri, M. & Robertson, J. Ab initio resonant Raman spectra of diamond-like carbons. *Diam. Relat. Mater.* **14**, 1078–1083 (2005).

55. Bokobza, L., Bruneel, J.-L. & Couzi, M. Raman Spectra of Carbon-Based Materials (from Graphite to Carbon Black) and of Some Silicone Composites. *C* **1**, 77–94 (2015).

56. Bhaumik, A. *et al.* Reduced Graphene Oxide Thin Films with Very Large Charge Carrier Mobility Using Pulsed Laser Deposition. *J. Mater. Sci. Eng.* **06**, (2017).

57. Wu, J.-B., Lin, M.-L., Cong, X., Liu, H.-N. & Tan, P.-H. Raman spectroscopy of graphene-based materials and its applications in related devices. *Chem. Soc. Rev.* **47**, 1822–1873 (2018).

58. Saito, R., Hofmann, M., Dresselhaus, G., Jorio, A. & Dresselhaus, M. S. Raman spectroscopy of graphene and carbon nanotubes. *Adv. Phys.* **60**, 413–550 (2011).

59. Tamor, M. A., Haire, J. A., Wu, C. H. & Hass, K. C. Correlation of the optical gaps and Raman spectra of hydrogenated amorphous carbon films. *Appl. Phys. Lett.* **54**, 123–125 (1989).

60. Tuinstra, F. & Koenig, J. L. Raman Spectrum of Graphite. *J. Chem. Phys.* **53**, 1126–1130 (1970).

61. Schwan, J., Ulrich, S., Batori, V., Ehrhardt, H. & Silva, S. R. P. Raman spectroscopy on amorphous carbon films. *J. Appl. Phys.* **80**, 440–447 (1996).

62. Lillo-Rodenas, M. A., Cazorla-Amoros, D. & Linares-Solano, A. Understanding chemical reactions between carbons and NaOH and KOH An insight into the chemical activation mechanism. 9 (2003).

63. Raymundo-Piñero, E., Azaïs, P., Cacciaguerra. T., Cazorla-Amorós, D., Linares-Solano, A. & Béguin, F. KOH and NaOH activation mechanisms of multiwalled carbon nanotubes with different structural organisation. *Carbon* **43**, 786–795 (2005).

64. Thommes, M. *et al.* Physisorption of gases, with special reference to the evaluation of surface area and pore size distribution (IUPAC Technical Report). *Pure Appl. Chem.* **87**, 1051–1069 (2015).

65. Brunauer, S., Emmett, P. H. & Teller, E. Adsorption of Gases in Multimolecular Layers. *J. Am. Chem. Soc.* **60**, 309–319 (1938).

66. Rouquerol, J. *et al.* Recommendations for the Characterization of Porous Solids. doi:10.1515/iupac.66.0925

67. Jagiello, J. & Olivier, J. P. 2D-NLDFT adsorption models for carbon slit-shaped pores with surface energetical heterogeneity and geometrical corrugation. *Carbon* **55**, 70–80 (2013).